Half widths of neutron spectra in dense helium-neon gas mixtures

P. Westerhuijs, L. A. de Graaf, and I. M. de Schepper
Interfaculty Reactor Institute, Delft University of Technology, 2629 JB Delft, The Netherlands
(Received 1 March 1993)

Results are presented of seven inelastic-neutron-scattering experiments on dense gas mixtures of helium and neon, performed on the Interfaculty Reactor Institute time-of-flight spectrometer RKS2. The concentration ratio of neon in the mixture is varied from 0 to 1 at 47 K and 285 bar. The neutron spectra $S(k,\omega)$, obtained for wave numbers $2.5 < k < 30$ nm^{-1}, are centered around the frequency $\omega=0$ with half widths $\omega_H(k)$. The experimental $\omega_H(k)$ agree well with the revised Enskog theory for equivalent binary hard-sphere fluid mixtures and show de Gennes minima similar to those in monoatomic fluids.

PACS number(s): 61.12.−q, 05.20.−y, 61.20.Lc

I. INTRODUCTION

It has been shown before [1] that the half width $\omega_H(k)$ of the experimentally observed (wave number k and frequency ω dependent) dynamic structure factor $S(k,\omega)$ of dense monoatomic fluids in equilibrium can be described very well by the revised Enskog theory [2] (RET) for equivalent hard-sphere fluids. Here the equivalent hard-sphere diameters σ are determined such that the static structure factors $S(k)$ of the monoatomic fluid and the hard-sphere gas (which are very similar) agree best. One finds for increasing number densities that $\omega_H(k)$ shows an increasingly deeper and more pronounced so-called de Gennes minimum at wave number $k=k^*\approx 2\pi/\sigma$, where $S(k)$ has its first maximum. This implies that plane-wave density fluctuations with k near k^* decay very slowly in time, which is the so-called "cage effect" [3]. One concludes from the good overall agreement between theory and experiment for $\omega_H(k)$ that the decay of such microscopic density fluctuations in simple dense monoatomic fluids is caused mainly by the strong repulsive (hard-sphere-like) part of the interparticle potentials. Thus, the cage effect is due to the hard core of the potential which causes the particles to be locked up in cages of size σ, corresponding to wave numbers $k^*\approx 2\pi/\sigma$. Therefore, $\omega_H(k^*)$, which is the inverse lifetime of a density fluctuation with wave number k^*, decreases with increasing density since the particles then become increasingly more locked up.

In this paper we make a similar comparison between theory and experiment for the half width $\omega_H(k)$ of practically the simplest of all binary mixtures: helium-neon. We do this to investigate whether the RET might also be useful to understand the basic microscopic dynamics of not-too-complicated dense binary mixtures in general. In particular, we study the de Gennes minimum in $\omega_H(k)$ for mixtures and its dependence on the total number density and concentration.

Seven neutron-scattering experiments on dense helium and neon gas mixtures have been performed ranging from pure helium to pure neon at temperatures near 47 K and pressures near 285 bar. In Table I we give for these seven states $He_{x_1}Ne_{x_2}$ the precise T and p; the partial number densities n_1, n_2; the total number density $n=n_1+n_2$; and the concentration $x_2=n_2/n$ (while $x_1=n_1/n=1-x_2$). Throughout this paper the label 1 refers to helium and 2 to neon.

We find that the measured $S(k)$ of all seven states are very much like those in equivalent hard-sphere mixtures. The equivalent hard-sphere diameters of helium ($\sigma_1=0.245$ nm) and neon ($\sigma_2=0.273$ nm) are obtained by fitting all experimental $S(k)$'s with the Percus-Yevick theory for hard-sphere fluid mixtures [4]. These diameters are used in the Enskog calculations of the half widths $\omega_H(k)$ of the $S(k,\omega)$'s for binary mixtures of hard spheres. It then appears that the theoretically calculated

TABLE I. Thermodynamic parameters of the seven experiments on mixtures of helium (1) and neon (2).

	T K	p bar	n_1 nm^{-3}	n_2 nm^{-3}	n nm^{-3}	x_2
He	46.9	284	23.3	0	23.3	0.00
$He_{0.78}Ne_{0.22}$	47.2	292	19.1	5.3	24.4	0.22
$He_{0.73}Ne_{0.27}$	47.3	283	18.1	6.7	24.8	0.27
$He_{0.37}Ne_{0.63}$	47.5	284	10.5	17.9	28.4	0.63
$He_{0.25}Ne_{0.75}$	47.0	283	7.2	22.0	29.2	0.75
$He_{0.08}Ne_{0.92}$	47.4	284	2.5	29.2	31.7	0.92
Ne	47.2	283	0	32.5	32.5	1.00

half widths are in good agreement with the experimental half widths for all wave numbers and all seven states. We observe a minimum in $\omega_H(k)$ for

$$k=k^*\approx 2\pi/\sigma_1\approx 2\pi/\sigma_2 ,$$

which becomes more pronounced when the total number density n increases. Thus we can conclude that the revised Enskog theory is also relevant to understand the basic dynamics in not-too-complicated binary mixtures. In particular, the decay of density fluctuations in dense binary mixtures like He-Ne might also be dominated by the strong repulsive hard-sphere-like parts of the interparticle potentials. Furthermore, we find that the half widths $\omega_H(k)$ of the He-Ne mixtures are very similar to those of a corresponding monoatomic fluid of hard spheres with average diameter $\sigma=(x_1\sigma_1^3+x_2\sigma_2^3)^{1/3}$ and average mass $m=x_1m_1+x_2m_2$ at the same total number density n and temperature T. Thus, for mixtures, the cage effect is again mainly geometrical in origin, i.e., determined by the diameters σ_1,σ_2 (which are close) and not so much by the large difference in masses m_1 and m_2 ($m_2=5m_1$).

In Sec. II we give a description of the experiments and the data reduction. In Sec. III we briefly outline the calculations to determine the dynamical structure factors for binary mixtures of hard spheres in equilibrium on the basis of the revised Enskog theory. In Sec. IV we present the experimental static structure factors $S(k)$ and the experimental half widths $\omega_H(k)$ of the $S(k,\omega)$'s and make a comparison between theory and experiment. In Sec. V we end with a short discussion of the results.

II. EXPERIMENTS AND DATA REDUCTION

The neutron-scattering experiments are performed on the rotating-crystal time-of-flight (TOF) spectrometer RKS2 at the 2-MW reactor of the Interfaculty Reactor Institute (IRI) in Delft. The pulsed monochromatic incident beam of neutrons on the sample had a cross section 2.5×10 cm^2 and an intensity $I_0=800$ neutrons cm^{-2}s^{-1}. The wavelength $\lambda_0=0.200$ nm of the neutrons (corresponding to an energy of $E_0=20.45$ meV) in the incident beam is selected by a rotating pyrolytic graphite crystal (18750 rpm) using the (004) Bragg reflection (Bragg angle $\theta_B=36.6°$). Reflections from other lattice planes are suppressed by two Fermi choppers in front of, and running in phase with, the crystal.

The sample container used in all experiments was a single aluminum cylinder with length 11 cm, diameter 2 cm, and wall thickness 0.1 cm subdivided into six parts with disks of boron nitride (a pure absorber) to reduce multiple scattering. This sample cell could sustain pressures up to 300 bar. Hence, the choice of pressures $p\approx 285$ bar given in Table I. The temperatures $T\approx 47$ K are chosen just above the critical temperature of neon (44 K) to avoid phase separation, but still allowing high densities.

While measuring the pressure, we first filled the sample container with purified neon and then with pure ^{4}He. The number densities of neon are then given by tabulated p-n-T data for neon [5] and the number densities of helium are derived from mass-spectroscopy measurements which agree with those calculated from the Van der Waals equation (Appendix A). In Table I, the density of the pure He state is taken from Ref. [6].

To determine the TOF spectra of scattered neutrons, we used 79 detectors located at a distance 1.503 m from the center of the sample at angles $-17.6°\le\phi\le 72.5°$ with $|\phi|\ge 4.4°$, and the spectra were recorded in 512 time channels of 1.55 μs width.

Our experiment consisted of seven sample runs in which the sample TOF spectra were determined and two dummy runs with corresponding TOF spectra. The first dummy run was for an empty container and the second for a container filled with a very small amount of ^{3}He gas (a pure and strong absorber). We used a straightforward interpolation of the two dummy measurements to determine the background spectrum of the empty container filled with that amount of ^{3}He that absorbs as many neutrons as the $\mathrm{He}_{x_1}\mathrm{Ne}_{x_2}$ sample scatters and absorbs.

To obtain the total dynamic structure factor $S(k,\omega)$ from these TOF spectra, we have used the correction programs of Ref. [7]. These programs corrected the spectra for the background, the efficiency of the detectors, the resolution of the spectrometer, and the self-shielding of the sample. They also normalize the spectra to a reference standard, and interpolate from constant scattering angle ϕ to constant wave number k. Finally, the spectra are symmetrized in ω using the quasiclassical approximation [7].

The resolution of the spectrometer was measured using a vanadium sample (vanadium is an incoherent scatterer) which had the same scattering geometry as the actual samples. These spectra were corrected for background, detector efficiency, and multiple scattering. The resolution function has an energy width at half maximum $\Delta E_0=1.3$ meV ($\Delta\omega_0=1.9$ ps^{-1}). The vanadium sample is also used for absolute normalization.

Thus we obtain the absolutely normalized symmetric total dynamic structure factor $S(k,\omega)$ of the He-Ne mixtures as a function of frequency ω for wave numbers $2.5<k<30$ nm^{-1}. The average measuring time was about 90 h per state. The pressure and temperature variation was less than 1% during the measurements.

The total dynamic structure factor is given by

$$S(k,\omega)=x_1b_1^{*2}S_{11}(k,\omega)+x_2b_2^{*2}S_{22}(k,\omega)+2(x_1x_2)^{1/2}b_1^*b_2^*S_{12}(k,\omega) , \quad (1)$$

with $x_1=n_1/(n_1+n_2)$ the number concentration of He, $x_2=n_2/(n_1+n_2)$ the number concentration of Ne, and b_j^* the normalized scattering length of species j, i.e.,

$$b_j^*=b_j/(x_1b_1^2+x_2b_2^2)^{1/2} , \quad (2)$$

with b_1 the scattering length of He and b_2 the scattering length of Ne. In Eq. (1) the $S_{jl}(k,\omega)$ are the partial dynamic structure factors given by

$$S_{jl}(k,\omega)=\frac{1}{2\pi}\int_{-\infty}^{\infty}dt\, e^{i\omega t}F_{jl}(k,t) , \quad (3)$$

with j or $l=1,2$, and the $F_{jl}(k,t)$ are the intermediate partial scattering functions

$$F_{jl}(k,t)=\langle \delta n_j(\mathbf{k},0)^*\delta n_l(\mathbf{k},t)\rangle \ . \tag{4}$$

Here the angular brackets denote the equilibrium canonical ensemble average, the asterisk denotes complex conjugation, $\mathbf{k}$ is a wave vector with length k, and $\delta n_l(\mathbf{k},t)$ is a microscopic plane-wave density fluctuation of species $l=1$ or 2 at time t, given for $\mathbf{k}\neq 0$ by

$$\delta n_l(\mathbf{k},t)=\frac{1}{\sqrt{N_l}}\sum_{p=1}^{N_l}\exp[i\mathbf{k}\cdot\mathbf{r}_l^{(p)}(t)] \ , \tag{5}$$

with N_l the number of particles of species l and $\mathbf{r}_l^{(p)}(t)$ the position of particle p of species l at time t.

The half width $\omega_H(k)$ of the total $S(k,\omega)$ as function of wave number k is defined by

$$S(k,\omega_H(k))=\tfrac{1}{2}S(k,0) \tag{6}$$

and is the decay frequency (or inverse lifetime) of a linear combination of He- and Ne-density fluctuations in the mixture. In fact, since $b_1=3.26$ fm and $b_2=4.55$ fm are not too different, $\omega_H(k)$ is practically the decay frequency of a fluctuation in the *total* number of He and Ne particles. We show this in Fig. 1 where we compare the coefficients $x_1b_1^{*2}$, $x_2b_2^{*2}$, and $2(x_1x_2)^{1/2}b_1^*b_2^*$ of the total $S(k,\omega)$ in Eq. (1) with those for the idealized case where He and Ne scatter equally, i.e., where $b_1=b_2$ or, equivalently, where $b_1^*=b_2^*=1$.

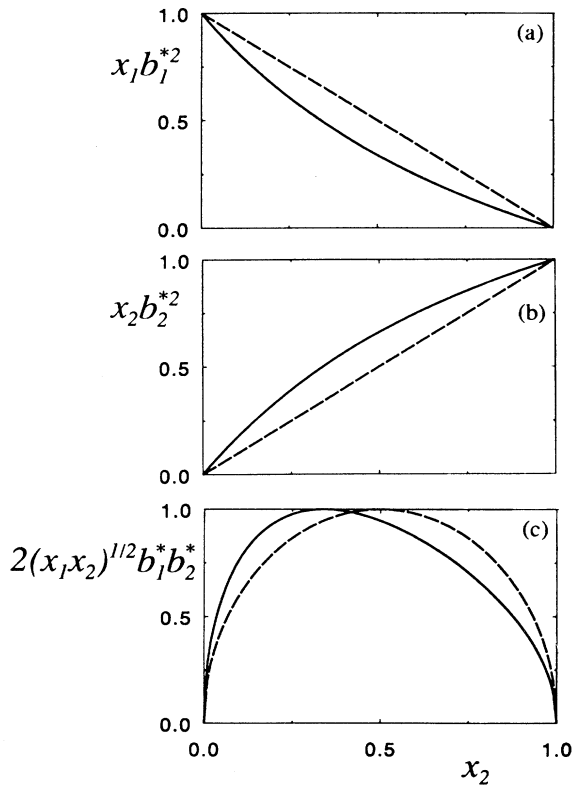

FIG. 1. The coefficients (a) $x_1b_1^{*2}$, (b) $x_2b_2^{*2}$, and (c) $2(x_1x_2)^{1/2}b_1^*b_2^*$ of Eq. (1) as functions of x_2 (solid curves). The dashed curves are for the idealized case of equal scattering $b_1=b_2$.

We show the experimental results for $\omega_H(k)$ (uncertainty $\pm 10\%$) in Sec. IV.

III. ENSKOG THEORY FOR BINARY MIXTURES

To understand the experimentally observed behavior of $\omega_H(k)$ as a function of k, concentration x_2, and total number density n, we use Enskog's theory for dense hard-sphere fluid mixtures. This so-called, revised Enskog theory (as revised by Van Beijeren and Ernst in 1973 [2]) is a natural and straightforward extension of Boltzmann's theory for dilute gas mixtures to higher densities n. Like the Boltzmann theory, the RET predicts all macroscopic quantities of a mixture (like the transport coefficients) and microscopic quantities [like $S(k,\omega)$] and expresses them in terms of the static properties of the full mixture in equilibrium and the dynamics of two isolated particles, while no adjustable parameters are involved. As such, the RET is a unique theory for dense mixtures, although it is restricted to hard-sphere model interactions only. The RET neglects the (small) effect of persistent correlations which occur between collisions at separated (long) time differences, i.e., the so-called mode-coupling contributions due to recollision effects [8]. Therefore, the RET is exact for short times (large ω), small distances (large k), and approximate (but reliable) in the remaining k-ω plane.

Using the revised Enskog theory for binary mixtures, the N-particle correlation functions $F_{jl}(\mathbf{k},t)$ of Eq. (4) are approximated by corresponding kinetic two-particle correlation functions $F_{jl}^E(\mathbf{k},t)\approx F_{jl}(\mathbf{k},t)$, which can be calculated numerically. This is achieved explicitly (as in the Boltzmann theory [9]) by first expressing the $F_{jl}(\mathbf{k},t)$ in terms of the single-particle nonequilibrium distribution functions $f_i(\mathbf{r},\boldsymbol{v},t)$ which give the number of particles of species 1 ($i=1$) and 2 ($i=2$) at $\mathbf{r}$ with velocity $\mathbf{v}$ at time t. Next, one assumes that the time evolution of the $f_i(\mathbf{r},\boldsymbol{v},t)$ is determined by the revised Enskog equation of Ref. [2]. As a result, the $F_{jl}^E(\mathbf{k},t)$ are for $t\geq 0$ given by ($j=1,2$ and $l=1,2$) [10,11]

$$F_{jl}^E(\mathbf{k},t)=\langle\langle \boldsymbol{\phi}_j(k)\cdot e^{tL^{E(\mathbf{k})}}\cdot\boldsymbol{\phi}_l(k)\rangle_1\rangle_2 \ . \tag{7}$$

Here the brackets $\langle\langle\ \rangle_1\rangle_2$ labeled 1 and 2 represent Gaussian averages over the velocities $\boldsymbol{v}_1$ and $\boldsymbol{v}_2$ and replace the N-particle average $\langle\ \rangle$ of Eq. (4):

$$\langle\langle\ \rangle_1\rangle_2=\int d\boldsymbol{v}_1\int d\boldsymbol{v}_2\phi^{(1)}(v_1)\phi^{(2)}(v_2)\cdots \ , \tag{8}$$

where

$$\phi^{(j)}(v)=\left[\frac{m_j}{2\pi k_BT}\right]^{3/2}\exp\left[\frac{-m_jv^2}{2k_BT}\right] \tag{9}$$

is the Maxwell velocity distribution for the species $j=1$ or 2, with k_B Boltzmann's constant, m_1 the mass of the He particles, and m_2 the mass of the Ne particles.

The (real) two-dimensional vectors $\boldsymbol{\phi}_j(k)$ and $\boldsymbol{\phi}_l(k)$ in Eq. (7) replace the (complex) densities $\delta n_j(\mathbf{k},0)^*$ and $\delta n_l(\mathbf{k},0)$, respectively, of Eq. (4) and are given by

$$\boldsymbol{\phi}_1(k)=[S_{11}(k)]^{1/2}\begin{bmatrix}\cos\alpha(k)\\ \sin\alpha(k)\end{bmatrix},$$
$$\boldsymbol{\phi}_2(k)=[S_{22}(k)]^{1/2}\begin{bmatrix}\sin\alpha(k)\\ \cos\alpha(k)\end{bmatrix}, \tag{10}$$

with

$$\alpha(k)=\tfrac{1}{2}\sin^{-1}\{S_{12}(k)/[S_{11}(k)S_{22}(k)]^{1/2}\}, \tag{11}$$

where the partial static structure factor

$$S_{jl}(k)=\int d\omega\, S_{jl}(k,\omega)=F_{jl}(k,0)$$

is the area of $S_{jl}(k,\omega)$ in Eq. (1). We note that in Eq. (7) for $t=0$,

$$F^E_{jl}(k,0)=F_{jl}(k,0)=S_{jl}(k),$$

which is a consequence of the fact that the RET is exact for short times.

The Enskog streaming operator $\exp\{tL^E(\mathbf{k})\}$ in Eq. (7) replaces the N-particle time evolution of Eq. (4) exactly up to order t^3 and approximately for $t\to\infty$. Here, the inhomogeneous Enskog operator $L^E(\mathbf{k})$ is a 2×2 matrix operator acting on two-dimensional vectors depending on $\boldsymbol{\nu}_1$ and $\boldsymbol{\nu}_2$ and transforming them into vectors of the same type. $L^E(\mathbf{k})$ is given by the sum of three 2×2 matrix operators, i.e.,

$$L^E(\mathbf{k})=V(\mathbf{k})+M(\mathbf{k})+\Lambda(\mathbf{k}). \tag{12}$$

Here, $V(\mathbf{k})$ is due to free streaming (as in an ideal-gas mixture). The mean-field operator $M(\mathbf{k})$ is a correction to free streaming, due to the fact that the partial static structure factors $S_{jl}(k)$ are not those of an ideal-gas mixture [where $S_{11}(k)=S_{22}(k)=1$ and $S_{12}(k)=0$]. The operator $\Lambda(\mathbf{k})$ is due to binary collisions. The matrix operators $V(\mathbf{k})$, $M(\mathbf{k})$, and $\Lambda(\mathbf{k})$ are given in Appendix B.

We obtain the partial dynamic structure factors $S_{jl}(k,\omega)$ in the Enskog theory from Eqs. (3) and (7), i.e.,

$$S_{jl}(k,\omega)=\frac{1}{\pi}\mathrm{Re}\left\langle\left\langle\boldsymbol{\phi}_j(k)\cdot\frac{-1}{i\omega+L^E(\mathbf{k})}\cdot\boldsymbol{\phi}_l(k)\right\rangle_1\right\rangle_2. \tag{13}$$

We evaluate these expressions numerically using the so-called Bhatnagar-Gross-Krook (BGK) approximation of order M ($=4,5,\ldots,\infty$). This BGK method, discussed in [12], treats the free-streaming term $V(\mathbf{k})$ and the mean-field operator $M(\mathbf{k})$ in Eq. (12) exactly for any M. In each step M the collision operator $\Lambda(\mathbf{k})$ in Eq. (12) is in fact approximated by a numerical $M\times M$ matrix consisting of the elements of this operator between the first M two-dimensional vectors in $\boldsymbol{\nu}_1$ and $\boldsymbol{\nu}_2$ of a complete ordered set. One finds that the BGK method converges rapidly when $M\geq10$ [12]. In the results presented in this paper we use $M=10$ throughout.

From the numerical results for $S_{jl}(k,\omega)$, we determine the half widths $\omega_H^{(1)}(k)$ of $S_{11}(k,\omega)$ and $\omega_H^{(2)}(k)$ of $S_{22}(k,\omega)$ defined by

$$S_{jj}[k,\omega_H^{(j)}(k)]=\tfrac{1}{2}S_{jj}(k,0)\quad(j=1,2) \tag{14}$$

and the half width $\omega_H(k)$ of the total dynamic structure factor $S(k,\omega)$ [cf. Eq. (1)] as defined in Eq. (6). We calculate the dynamical structure factors and the half widths for the seven experimental states using the parameters given in Table I. All the results are given in Sec. IV. Here we discuss their general behavior, as illustrated by the results of the state $He_{0.37}Ne_{0.63}$.

In Fig. 2 we show for $He_{0.37}Ne_{0.63}$ the half widths $\omega_H^{(1)}(k)$, $\omega_H^{(2)}(k)$, and $\omega_H(k)$ as a function of k. We consider their large- and small-k behavior separately.

For *large* k (≥20 nm^{-1}), one observes in Fig. 2 a tendency of the half widths $\omega_H^{(1)}(k)$ and $\omega_H^{(2)}(k)$ towards the corresponding ideal-gas values, i.e.,

$$\omega_H^{(1)}(k)=\left(\frac{2\ln2}{\beta m_1}\right)^{1/2}k[1+O(k^{-1})],$$
$$\omega_H^{(2)}(k)=\left(\frac{2\ln2}{\beta m_2}\right)^{1/2}k[1+O(k^{-1})] \tag{15}$$
$$(k\to\infty).$$

One also observes in Fig. 2 a tendency of $\omega_H(k)$ to its corresponding ideal-gas behavior $\omega_H(k)$ $(k\to\infty)$ that is calculated numerically from Eqs. (1) and (6) using the fact that $S_{11}(k,\omega)$ and $S_{22}(k,\omega)$ are, for $k\to\infty$, ideal-gas Gaussians in ω, while $S_{12}(k,\omega)=0$ then. The results for $\omega_H(k)$ $(k\to\infty)$ are shown in Fig. 3 as a function of x_2. One sees that $\omega_H(\infty)$ is always intermediate between $\omega_H^{(1)}(\infty)$ and $\omega_H^{(2)}(\infty)$ and very close to $\omega_H^{(2)}(\infty)$ for $x_2\geq0.5$.

Thus we can understand, in part, the general global behavior of the half widths $\omega_H^{(1)}(k)$, $\omega_H^{(2)}(k)$, and $\omega_H(k)$ predicted by the Enskog theory for *large* k (≥20 nm^{-1}), namely, that

$$\omega_H^{(2)}(k)<\omega_H(k)<\omega_H^{(1)}(k). \tag{16}$$

This basic relation follows from the fact that $\omega_H^{(2)}(k)$ is (much) smaller than $\omega_H^{(1)}(k)$ since in Eq. (15) the thermal speed $(\beta m_2)^{-1/2}$ of the heavy Ne particles is (much) smaller than the thermal speed $(\beta m_1)^{-1/2}$ of the light He particles. Furthermore, $\omega_H(k)$ is intermediate between

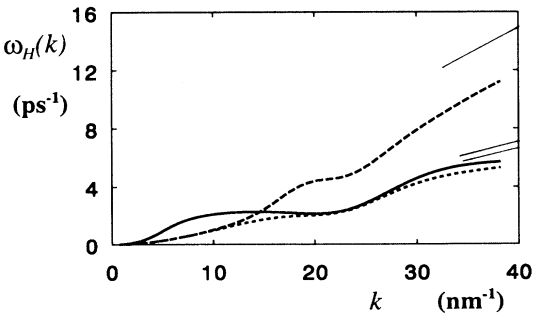

FIG. 2. Theoretical Enskog half widths $\omega_H^{(1)}(k)$ (upper dashed curve), $\omega_H(k)$ (solid curve), and $\omega_H^{(2)}(k)$ (lower dashed curve) as functions of k for $He_{0.37}Ne_{0.63}$. The solid straight lines at large k are the corresponding ideal-gas predictions for $\omega_H^{(1)}(k)$, $\omega_H(k)$, and $\omega_H^{(2)}(k)$ (from top to bottom).

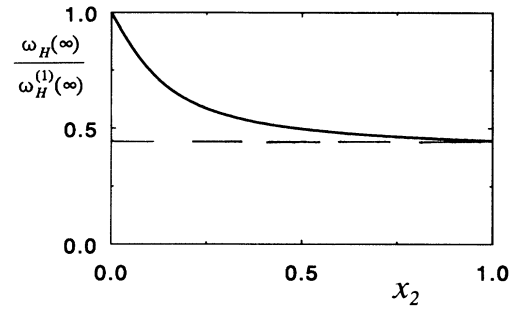

FIG. 3. Reduced half width $\omega_H(\infty)/\omega_H^{(1)}(\infty)$ as function of x_2 (solid curve). The dashed straight line is $\omega_H^{(2)}(\infty)/\omega_H^{(1)}(\infty)$ so that $\omega_H^{(2)}(\infty) < \omega_H(\infty) < \omega_H^{(1)}(\infty)$ [cf. Eq. (16)].

$\omega_H^{(1)}(k)$ and $\omega_H^{(2)}(k)$, which is an exact consequence of Eq. (1) as long as $S_{12}(k,\omega)$ is negligibly small (as in ideal gases).

The rather obvious and "natural" behavior of the half widths given by Eq. (16) is further illustrated in Fig. 4. There we show the Enskog results for $S_{jl}(k,\omega)$ and $S(k,\omega)$ as a function of ω at $k=20$ nm^{-1} for $He_{0.37}Ne_{0.63}$. One observes in Fig. 4 that $S_{12}(k,\omega)$ is very small indeed and that $S_{11}(k,\omega)$ and $S_{22}(k,\omega)$ show a Gaussian behavior in ω, with very different half widths $\omega_H^{(2)}(k) \ll \omega_H^{(1)}(k)$, due to the differences in masses. Thus, Eq. (16) is clearly satisfied.

For *small* k ($k \leq 12$ nm^{-1}), one observes in Fig. 2 a completely different, and not so immediately obvious, behavior for the half widths. From the Enskog theory we find for *small* k that

$$\omega_H^{(1)}(k) = \omega_H^{(2)}(k) \ll \omega_H(k) \ . \tag{17}$$

Thus, peculiarly, the half width of the total $S(k,\omega)$ in Eq. (1) is much *larger* than the half widths of $S_{11}(k,\omega)$ and $S_{22}(k,\omega)$, which are equal. We illustrate this behavior in Fig. 4. There we show the Enskog results for $S_{jl}(k,\omega)$ and $S(k,\omega)$ at $k=2$ nm^{-1} for $He_{0.37}Ne_{0.63}$. One sees in Fig. 4 sharp central positive peaks in $S_{11}(k,\omega)$ and $S_{22}(k,\omega)$ with equal widths $\omega_H^{(1)}(k)=\omega_H^{(2)}(k)$ which cancel in the total $S(k,\omega)$ the strong sharp negative contribution in $S_{12}(k,\omega)$, so that

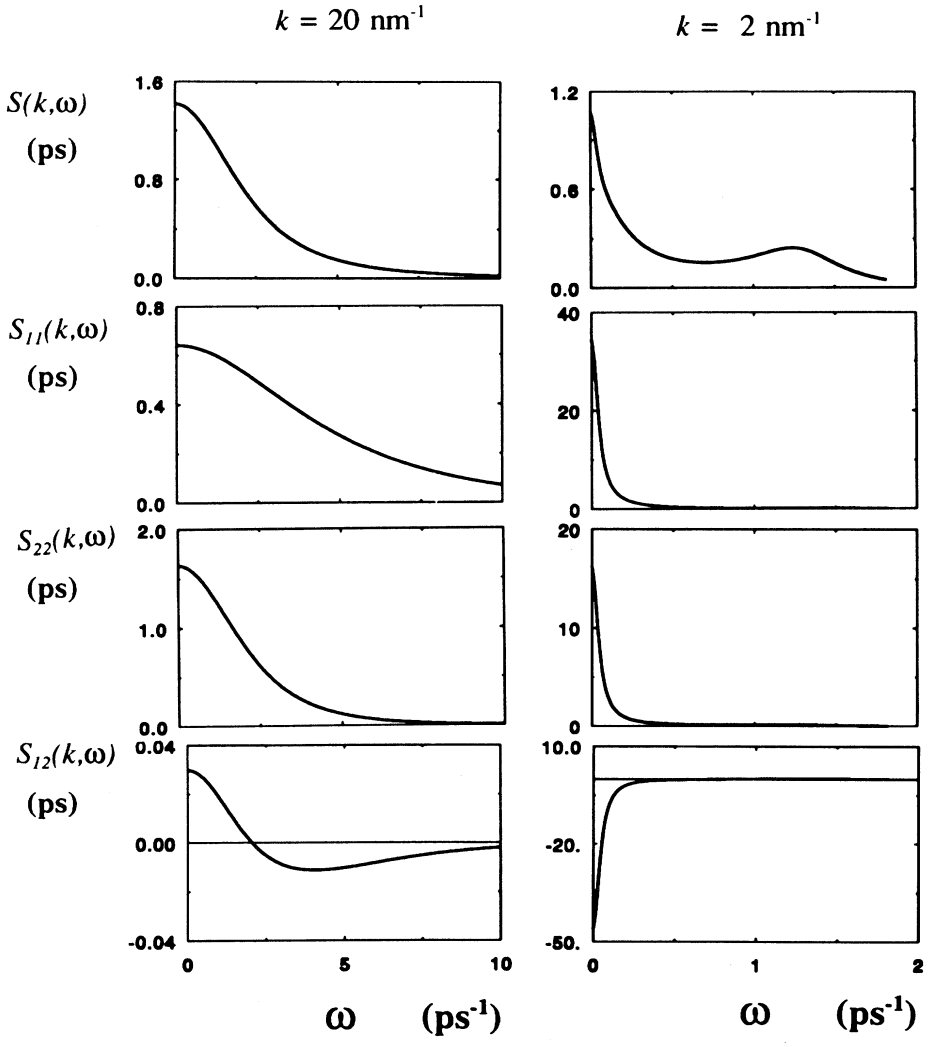

FIG. 4. Theoretical Enskog results ($He_{0.37}Ne_{0.63}$) for $S(k,\omega)$, $S_{11}(k,\omega)$, $S_{22}(k,\omega)$, and $S_{12}(k,\omega)$ as functions of ω (solid curves). Left column: $k=20$ nm^{-1}. Note that $S_{12}(k,\omega)$ is very small and that $\omega_H^{(2)}(k) < \omega_H(k) < \omega_H^{(1)}(k)$ [cf. Eq. (16)]. Right column: $k=2$ nm^{-1}. Note that $S_{12}(k,\omega)$ is strongly negative and that $\omega_H^{(2)}(k)=\omega_H^{(1)}(k) \ll \omega_H(k)$ [cf. Eq. (17)]. The side peak in $S(k,\omega)$ at $\omega=1.3$ ps^{-1} ($\approx c_E k$) is due to the sound mode.

TABLE II. Enskog values for the heat diffusion a_E, the concentration diffusion D_E, the sound damping Γ_E, and the sound velocity c_E (c is the actual sound velocity and c_{vdW} that from the van der Waals equation). The total reduced density $n^*=n_1\sigma_1^3+n_2\sigma_2^3$ and l^{-1} is the inverse averaged mean free path. a is the actual heat diffusion.

		l^{-1}	a	a_E	D_E	Γ_E	c_E	c_{vdW}	c
	n^*	nm^{-1}		(10^{-2} nm^2/ps)			ms^{-1}	ms^{-1}	ms^{-1}
He	0.34	10.1	11.3	11.7	1.94	11.1	841	788	750
$He_{0.78}Ne_{0.22}$	0.39	12.3		8.7	1.68	11.6	679	587	
$He_{0.73}Ne_{0.27}$	0.40	12.7		8.2	1.60	11.0	666	565	
$He_{0.37}Ne_{0.63}$	0.52	19.7		6.5	1.16	8.7	671	504	
$He_{0.25}Ne_{0.75}$	0.55	21.8		6.4	1.08	8.6	680	485	
$He_{0.08}Ne_{0.92}$	0.63	28.7		7.1	0.92	10.2	767	551	
Ne	0.66	31.7	5.4	7.7	0.86	11.1	802	578	571

$$\omega_H^{(1)}(k)=\omega_H^{(2)}(k)\ll\omega_H(k)$$

indeed.

Physically, Eq. (17) can be understood from hydrodynamics, valid for $k\to 0$. For small k, the Enskog operator $L^E(\mathbf{k})$ of Eq. (12) has *four* hydrodynamic eigenmodes, i.e., eigenvectors $\psi_\mu(\mathbf{k})$ and corresponding eigenvalues $z_\mu(k)$ (which vanish for $k=0$), labeled $\mu=c,h,+,-$,

$$L^E(\mathbf{k})\Psi_\mu(\mathbf{k})=-z_\mu(k)\Psi_\mu(\mathbf{k})\ . \tag{18}$$

Here, $\mu=c$ refers to the concentration diffusion mode, $\mu=h$ to the heat mode, and $\mu=+$ and $-$ to the two sound modes. These four hydrodynamic eigenmodes of $L^E(\mathbf{k})$ determine all $S_{jl}(k,\omega)$ for $k\to 0$ completely.

The eigenvalues are for small k given by

$$\begin{aligned} z_c(k)&=D_Ek^2+O(k^4)\ ,\\ z_h(k)&=a_Ek^2+O(k^4)\ ,\\ z_\pm(k)&=\pm ic_Ek+\Gamma_Ek^2+O(k^3)\ , \end{aligned} \tag{19}$$

where D_E is the concentration diffusion coefficient, a_E the heat diffusivity, c_E the hydrodynamic speed of sound and Γ_E the sound damping. These (Enskog) parameters are given in Table II and in Fig. 5, where one sees that $a_E\gg D_E$, as is typical for dense fluid mixtures.

It follows from Eqs. (18) and (13) that all partial dynamic structure factors $S_{jl}(k,\omega)$ are given by a sum of four Lorentzian lines ($k\to 0$):

$$S_{jl}(k,\omega)=\frac{1}{\pi}\mathrm{Re}\sum_{\mu=c,h,+,-}\frac{A_{jl}^{(\mu)}(k)}{-i\omega+z_\mu(k)}\ , \tag{20}$$

with amplitudes given by

$$A_{jl}^{(\mu)}(k)=\left\langle\left\langle\phi_j(\mathbf{k})\cdot\Psi_\mu(\mathbf{k})\right\rangle_1\right\rangle_2\left\langle\left\langle\Psi_\mu(\mathbf{k})\cdot\phi_l(\mathbf{k})\right\rangle_1\right\rangle_2\ . \tag{21}$$

Therefore, in all three $S_{jl}(k,\omega)$ and in the total $S(k,\omega)$, there are two Brillouin lines located at $\pm c_Ek$ with equal half width Γ_Ek^2 due to the two sound modes, one central line with half width $z_c(k)=D_Ek^2$ due to the concentration diffusion mode, and one central line with half width $z_h(k)=a_Ek^2$ due to the heat mode. The sound modes are not very relevant for the half widths, since they appear in the sidewings of $S_{jl}(k,\omega)$. In practice, the half widths are determined by an interplay of the amplitude $A_{jl}^{(c)}(k)$ of the (narrow) central concentration-diffusion-mode contribution and the amplitude $A_{jl}^{(h)}(k)$ of the (broad) central heat-mode contribution. We find for all three $S_{jl}(k,\omega)$

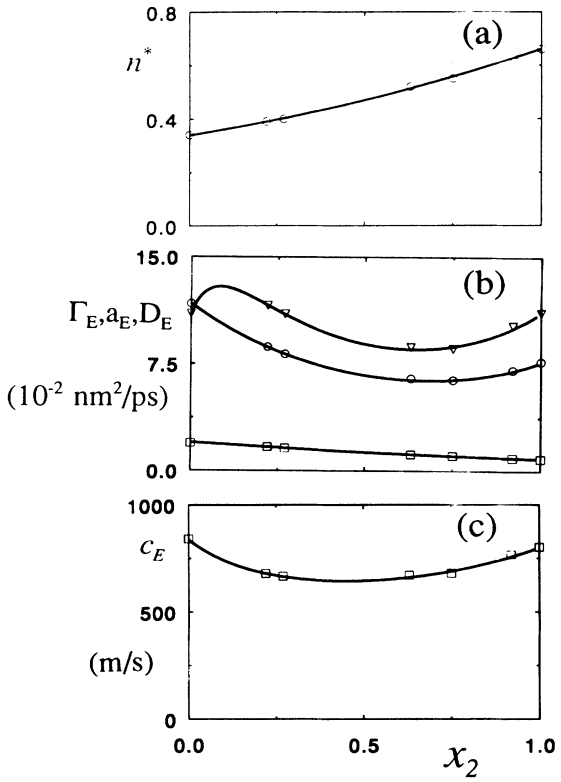

FIG. 5. Total reduced density $n^*=n_1\sigma_1^3+n_2\sigma_2^3$ as a function of x_2 for the states $He_{x_1}Ne_{x_2}$ of Table I [open circles in (a)]. The solid curve in (a) is a smooth interpolation. Enskog sound damping Γ_E [triangles in (b)], heat diffusion a_E [circles in (b)], concentration diffusion coefficients D_E [squares in (b)], and sound velocity c_E [squares in (c)], as functions of x_2, for $He_{x_1}Ne_{x_2}$ (cf. Table II). The solid curves in (b) and (c) are theoretical, using n^* as a function of x_2 from (a).

that the amplitudes $A_{jl}^{(c)}(k)$ of the concentration diffusion mode are considerable so that for $k \to 0$,

$$\omega_H^{(1)}(k)=\omega_H^{(2)}(k)=z_c(k)=D_E k^2 . \quad (22)$$

For the total $S(k,\omega)$ we find a negligible contribution of the concentration diffusion mode. This is due to the fact that in $S(k,\omega)$ fluctuations in the *total* number of particles are mainly observed as discussed under Eq. (6). Therefore, the central part of $S(k,\omega)$ is determined dominantly by the heat mode (which includes these fluctuations in the total number of particles). Hence, for $k \to 0$,

$$\omega_H(k)=z_h(k)=a_E k^2 , \quad (23)$$

so that $\omega_H(k)$ is much larger than $\omega_H^{(1)}(k)=\omega_H^{(2)}(k)$ since $a_E \gg D_E$ (see Fig. 5). We conclude therefore that the behavior of the half widths given by Eq. (17) is typical for hydrodynamics, due to the fact that in dense fluid mixtures the heat diffusion coefficient a is much larger than the concentration diffusion coefficient D.

We find from the Enskog theory for mixtures with $0<x_2<1$ that the hydrodynamiclike behavior given by Eq. (17) occurs when $kl<1$ ($k<l^{-1}$; the particles undergo "many" collisions over long distances), while the ideal-gas-like behavior given by Eq. (16) holds when $kl>1$ ($k>l^{-1}$; the particles move "freely" over short distances). Here, l is the averaged mean free path between collisions in the binary mixture, defined as the mean free path in the corresponding simple fluid with total number density $n=n_1+n_2$ and averaged diameter $\sigma=(x_1\sigma_1^3+x_2\sigma_2^3)^{1/3}$. The values of l^{-1} are given in Table II.

As can be read in Table II, the Enskog theory yields realistic values for the actual sound velocity c and heat diffusivity a [13], implying that the theory might be representative for the real $He_{x_1}Ne_{x_2}$ mixtures in the hydrodynamic region ($k \to 0$). In Sec. IV we compare the theoretical Enskog results for $\omega_H(k)$ with experiment for microscopic k values of the order of l^{-1}.

IV. EXPERIMENTAL AND THEORETICAL RESULTS

In this section we present the experimental and theoretical results for the total static structure factors $S(k)$ and the half widths $\omega_H(k)$ of the total dynamic structure factors $S(k,\omega)$ for the seven $He_{x_1}Ne_{x_2}$ states given in Table I. We start with the total static structure

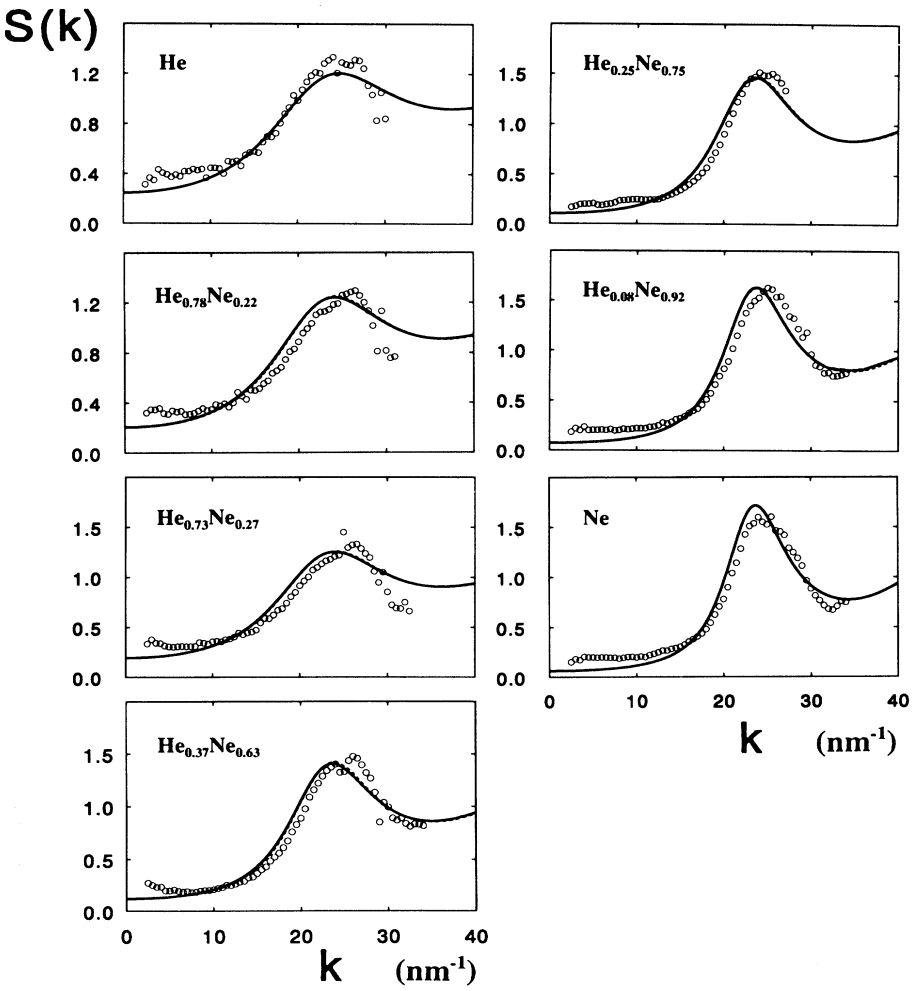

FIG. 6. Total experimental static structure factors $S(k)$ as functions of k for the $He_{x_1}Ne_{x_2}$ mixtures of Table I (open circles). The solid curves are from the Percus-Yevick theory for corresponding binary mixtures of hard spheres and the dashed curves for corresponding monoatomic fluids of hard spheres. The solid and dashed curves are virtually indistinguishable.

factor $S(k)$ given by [cf. Eq. (1)]

$$S(k)=\int_{-\infty}^{\infty} d\omega\, S(k,\omega)$$
$$=x_1 b_1^{*2} S_{11}(k)+x_2 b_2^{*2} S_{22}(k)$$
$$+2(x_1x_2)^{1/2} b_1^* b_2^* S_{12}(k)\ . \quad (24)$$

In Fig. 6 the seven experimental $S(k)$'s are plotted as a function of k. One observes in Fig. 6 that the first peak in $S(k)$ at $k=k^*\approx 23$ nm^{-1} gets more pronounced when x_2 increases from 0 to 1 (top to bottom). We find that the experimental $S(k)$'s are similar to those of hard-sphere mixtures. From the experimental $S(k)$'s we obtained equivalent hard-sphere diameters of the helium and neon particles by fitting with the theoretical Percus-Yevick hard-sphere-mixture $S(k)$'s [4]. Simultaneous best fits are obtained when $\sigma_1=0.245$ nm and $\sigma_2=0.273$ nm. The hard-sphere Percus-Yevick $S(k)$'s (using these best-fit diameters) are shown in Fig. 6, as solid curves. We also find that the Percus-Yevick-mixture $S(k)$'s are virtually indistinguishable from those in an equivalent *monoatomic* fluid of hard spheres with diameter $\sigma=(x_1\sigma_1^3+x_2\sigma_2^3)^{1/3}$ at the same density n (Fig. 6). Thus, also, the reduced densities $n^*=n\sigma^3=n_1\sigma_1^3+n_2\sigma_2^3$ are the same in the mixture and the monoatomic fluid. Therefore, we conclude that when x_2 increases, the peak in $S(k)$ becomes more pronounced due to the increase in reduced density n^*, rather than in x_2 (cf. Table II).

Next we present the experimental results for the half widths $\omega_H(k)$ of the total $S(k,\omega)$. For all states the experimental $\omega_H(k)$ are plotted in Figs. 7 and 8 (left columns) as a function of k. All half widths tend to have a minimum at $k^*\approx 20$ nm^{-1} corresponding to where $S(k)$ has a maximum (see Fig. 6). Also, one observes in Figs. 7 and 8 that the minimum in $\omega_H(k)$ near 20 nm^{-1} becomes more pronounced when the total reduced density $n^*=n_1\sigma_1^3+n_2\sigma_2^3$ increases (from He to Ne; see Table II). In addition, the minimum value $\omega_H(k^*)$ decreases with increasing n^*. This can be seen most clearly in Fig. 9(a) where we plot $\omega_H(k^*)$ as a function of n^*.

The solid curves in the figures in the left columns of Figs. 7 and 8 are the theoretical results for $\omega_H(k)$ of the Enskog calculations (see Sec. III). For all states the Enskog half widths agree well with experiment—in particular, at small k values (for most mixture states up to 10 nm^{-1}) and at the k values around 20 nm^{-1} where $S(k)$ has its maximum. One notices that the increasingly more pronounced minima in the experimental $\omega_H(k)$ with in-

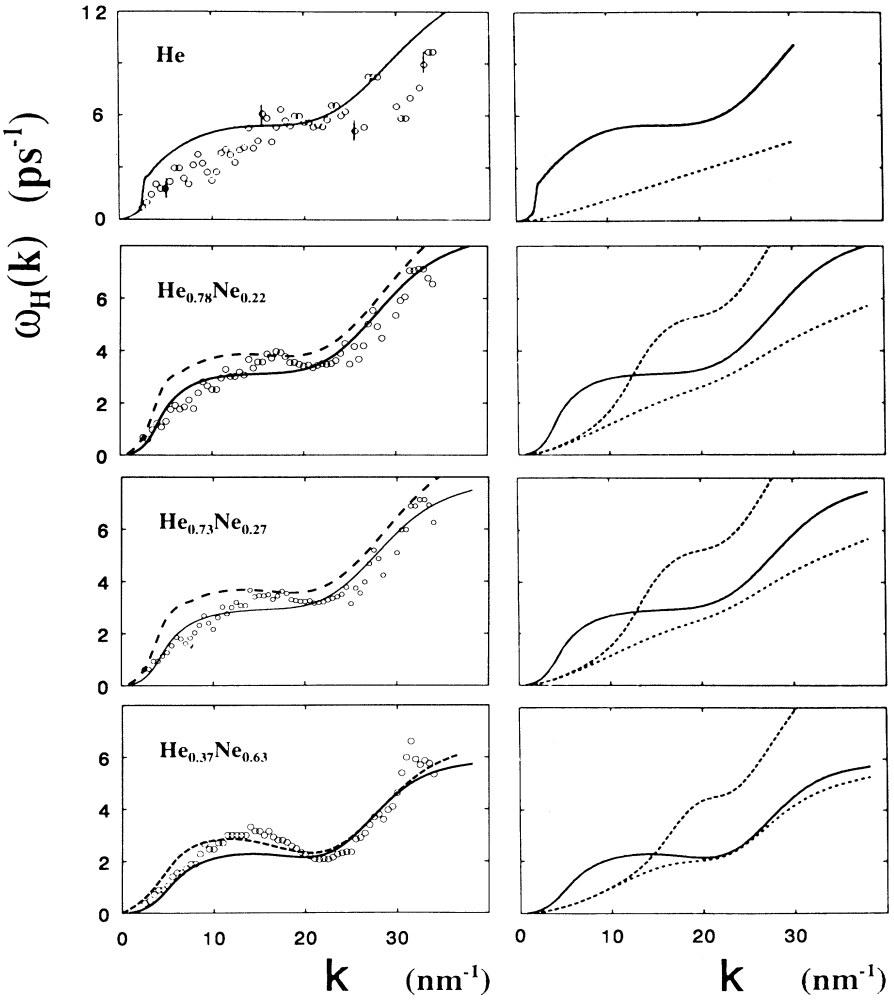

FIG. 7. Half widths $\omega_H(k)$ of the total dynamic structure factors as functions of k for the He-Ne experiments with $x_2=0$, 0.22, 0.27, and 0.63 of Table I (open circles in the left column). The dashed curves in the left column are the $\omega_H^m(k)$ of the corresponding monoatomic hard-sphere fluids. The solid curves in the left and right columns are from the Enskog theory for corresponding binary mixtures of hard spheres. In the right column the upper dashed curves are the theoretical $\omega_H^{(1)}(k)$ for the He component and the lower dashed curves are the theoretical $\omega_H^{(2)}(k)$ for the Ne component. For $x_2=0$, the dashed curve is for one neon particle in pure helium. The jump in $\omega_H(k)=\omega_H^{(1)}(k)$ at $k=2$ nm^{-1} is due to interference of the sound mode with the central line.

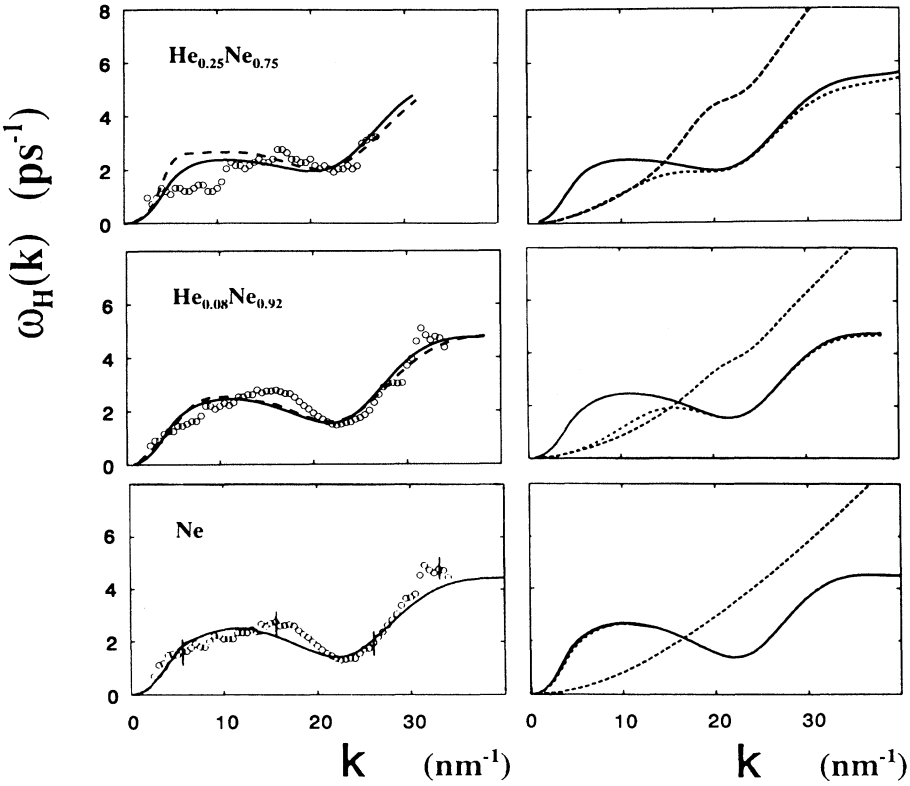

FIG. 8. Half widths $\omega_H(k)$ of the total dynamic structure factors as functions of k for the He-Ne experiments with $x_2=0.75$, 0.92, and 1.0 of Table I (open circles in the left column). The dashed curves in the left column are the $\omega_H^m(k)$ of the corresponding monoatomic hard-sphere fluids. The solid curves (left and right columns) are from the Enskog theory for corresponding binary mixtures of hard spheres. Right column, $x_2\neq 1$ and $k>20$ nm^{-1}; the upper and lower dashed curves are the theoretical $\omega_H^{(1)}(k)$ for the He component and $\omega_H^{(2)}(k)$ for the Ne component, respectively. Right column, $x_2=1$; the dashed curve $[\omega_H^{(1)}(k)]$ is for one helium particle in pure neon.

creasing n^* are well represented by the theoretical calculations. To study how the $\omega_H(k)$ of mixtures are similar to those of monoatomic fluids, we have calculated the half widths $\omega_H^m(k)$ of the corresponding monoatomic fluids of hard spheres [diameter $\sigma=(x_1\sigma_1^3+x_2\sigma_2^3)^{1/3}$ and mass $m=x_1m_1+x_2m_2$]. The results are shown in Figs. 7 and 8 (dashed curves in the left columns). One sees that the $\omega_H(k)$ of the $He_{x_1}Ne_{x_2}$ mixtures are indeed similar to the $\omega_H^m(k)$ of monoatomic fluids. In particular, the deepening and sharpening of the de Gennes minimum with increasing n^* seen in mixtures is virtually the same as that observed in simple fluids. This is further illustrated in Fig. 9(b) where we plot the reduced $\omega_H(k^*)t_\sigma$ and $\omega_H^m(k)t_\sigma$ as functions of n^*. Here, $t_\sigma=\frac{1}{2}(\beta m)^{1/2}\sigma$ is the average time an average particle needs to transverse σ with average thermal speed $(\beta m)^{-1/2}$. We conclude from Fig. 9(b) that the effect of de Gennes narrowing is virtually the same in He-Ne mixtures and in simple monoatomic fluids.

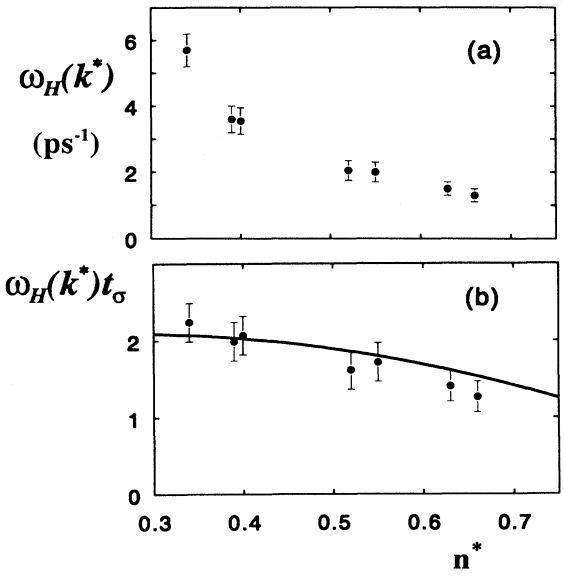

FIG. 9. Experimental half widths $\omega_H(k^*)$ for $k=k^*$ as a function of n^* for the seven He-Ne mixtures of Table I [solid circles in (a)]. In (b) the experimental reduced half widths (solid circles) are compared with the theoretical prediction (solid curve) for corresponding monoatomic fluids of hard spheres.

In the figures in the right columns of Figs. 7 and 8, the solid curve is again the theoretical Enskog half width $\omega_H(k)$. The dashed curves are the theoretical half widths $\omega_H^{(i)}(k)$ of the partial dynamic structure factors $S_{ii}(k,\omega)$ [$i=1$ for helium and $i=2$ for neon; see Eq. (17)].

Apparently, for increasing $x_2>0.2$ the theoretical half widths $\omega_H(k)$ are increasingly determined by the neon contribution $S_{22}(k,\omega)$ when $k>l^{-1}$, with l the averaged mean free path between collisions (see Table II), and then satisfy the basic relation

$$\omega_H^{(2)}(k)<\omega_H(k)\ll\omega_H^{(1)}(k)$$

[Eq. (16)]. For small k ($k<l^{-1}$) one observes in Figs. 7 and 8 the typical hydrodynamiclike behavior

$$\omega_H^{(1)}(k)=\omega_H^{(2)}(k)\ll\omega_H(k)$$

[Eq. (17)]. Therefore, for $k<l^{-1}$, $\omega_H(k)$ is determined

by heat diffusion $\omega_H(k) \approx a_E k^2$ and not by the helium or neon components that both behave as

$$\omega_H^{(1)}(k) = \omega_H^{(2)}(k) \approx D_E k^2 .$$

Due to the good agreement between theory and experiment, we expect also that the experimental $\omega_H(k)$ are dominated by the neon contribution for $k > l^{-1}$ and by collective heat diffusion for $k < l^{-1}$. This conclusion differs from that in Ref. [14] where it was conjectured that the experimental half widths $\omega_H(k)$ are dominated by the neon particles for all microscopic k relevant in neutron scattering.

V. DISCUSSION

We find that the experimental half widths $\omega_H(k)$ for seven neutron spectra of He-Ne mixtures agree well with the revised Enskog theory. The agreement is the more surprising since no adjustable parameters are involved in the comparison. Thus we have established the relevance of the revised Enskog theory for dense binary mixtures on the microscopic level, i.e., for wave numbers k corresponding to distances of the order of interparticle separations.

Due to the good agreement for $\omega_H(k)$, one can have some confidence in the predictions of the RET for the dynamics of the separate He and Ne components in the mixture, i.e., for the corresponding $\omega_H^{(1)}(k)$ and $\omega_H^{(2)}(k)$, respectively. Over *short* distances ($k > l^{-1}$) the light He particles move much faster than the heavy Ne particles so that $\omega_H^{(2)}(k) \ll \omega_H^{(1)}(k)$ [Eq. (16)]. Over *long* distances ($k < l^{-1}$) the He and Ne particles move *equally* fast:

$$\omega_H^{(1)}(k) = \omega_H^{(2)}(k) \approx D_E k^2 ,$$

with D_E the concentration diffusion coefficient [Eq. (22)]. Clearly, a He (or Ne) particle can move around only when its emptied space is filled with a Ne (or He) particle whereby the total density is constant.

According to the RET, the experimentally observed half width $\omega_H(k)$ is the decay frequency of a fluctuation in the total number of He and Ne particles. Therefore, for small k ($k < l^{-1}$), $\omega_H(k) \approx a_E k^2$ [with a_E the heat diffusivity; see Eq. (23)] is much larger than

$$\omega_H^{(1)}(k) = \omega_H^{(2)}(k) \approx D_E k^2 .$$

It appears that a fluctuation in the total number of particles relaxes fast due to the fact that the particles can push each other away, as in heat diffusion (they do not have to pass each other, as in concentration diffusion). For large k ($k > l^{-1}$), $\omega_H(k)$ is dominated by the slow-moving Ne particles so that

$$\omega_H^{(2)}(k) < \omega_H(k) \ll \omega_H^{(1)}(k) .$$

In the transition from small-k to large-k behavior, $\omega_H(k)$ develops a de Gennes minimum near $k \approx 20$ nm^{-1} (see Figs. 7 and 8), the behavior of which is very similar to that observed in simple monoatomic fluids [see Fig. 9(b)].

Unfortunately, the peculiar theoretical predictions for $\omega_H^{(1)}(k)$ and $\omega_H^{(2)}(k)$ cannot be tested with neutron scattering on He-Ne mixtures since there are no appropriate isotopes. However, they have been verified recently from molecular-dynamics simulations of He-Ne mixtures [15]. A verification could also come from neutron scattering on mixtures like He-Ar, since the isotopes ^{36}Ar and ^{40}Ar of Ar scatter in a vastly different manner. For such mixtures all three halfwidths $\omega_H^{(1)}(k)$, $\omega_H^{(2)}(k)$, and $\omega_H(k)$ can be determined experimentally and tested with theory.

APPENDIX A: THE VAN DER WAALS EQUATION FOR BINARY MIXTURES

The van der Waals model for binary mixtures, sometimes called the one-fluid model, is used to determine the composition of the He-Ne mixture states and to estimate the sound velocity. Here, the van der Waals equation of state for mixtures reads [16]

$$p = \frac{n k_B T}{1 - n b_{\mathrm{vdW}}} - a_{\mathrm{vdW}} n^2 , \tag{A1}$$

with $n = n_1 + n_2$ the total number density of the mixture. The parameters a_{vdW} and b_{vdW} are given by

$$\begin{aligned} a_{\mathrm{vdW}} &= a_{11} x_1^2 + 2 a_{12} x_1 x_2 + a_{22} x_2^2 , \\ b_{\mathrm{vdW}} &= b_{11} x_1^2 + 2 b_{12} x_1 x_2 + b_{22} x_2^2 . \end{aligned} \tag{A2}$$

Here, $x_1 = n_1/n$, $x_2 = n_2/n$, and the parameters a_{11}, b_{11} and a_{22}, b_{22} and the van der Waals parameters of *pure* helium and *pure* neon, respectively. The cross-coefficients a_{12} and b_{12} are functions of the pure fluid parameters

$$a_{12} = (a_{11} a_{22})^{1/2} \tag{A3}$$

and

$$b_{12} = \tfrac{1}{8} (b_{11}^{1/3} + b_{22}^{1/3})^3 . \tag{A4}$$

From tabulated p-n-T data for pressures p near 280 bar and temperatures T near 47 K, we determined the coefficients a_{ii} and b_{ii} ($i = 1,2$) (Refs. [5,6]) for pure helium (1) and pure neon (2). For helium, we find

$$a_{11} = 0.361 \times 10^{-23} \text{ J nm}^3$$

($= 0.0361$ nm^6 bar), $b_{11} = 0.0215$ nm^3 and for neon,

$$a_{22} = 4.76 \times 10^{-23} \text{ J nm}^3$$

($= 0.476$ nm^6 bar), $b_{22} = 0.0226$ nm^3. From these data we calculate the concentrations x_2 given in Table I.

We determine the sound velocity c_{vdW} from

$$c_{\mathrm{vdW}} = \left[\frac{\gamma}{m n \kappa_T} \right]^{1/2} , \tag{A5}$$

with $m = x_1 m_1 + x_2 m_2$ the averaged mass of a particle, $\kappa_T = (\partial n / \partial p)_T / n$ the isothermal compressibility, and $\gamma = c_p / c_v$ the ratio of specific heats per particle at constant pressure (c_p) and constant volume (c_v) that satisfies the thermodynamic relation

$$\gamma = 1 + \frac{T \alpha^2}{n \kappa_T c_v} , \tag{A6}$$

with $\alpha=-(\partial n/\partial T)_p/n$ the thermal expansion coefficient. To obtain c_{vdW}, we calculate κ_T and α from Eq. (A1) and we use that in the van der Waals theory $c_v=3k_B/2$, as in an ideal gas. The results for c_{vdW} are given in Table II.

APPENDIX B: THE ENSKOG OPERATOR

We give the explicit expression for the inhomogeneous Enskog operator $L^E(\mathbf{k})$ of Eq. (12), i.e.,

$$L^E(\mathbf{k})=V(\mathbf{k})+M(\mathbf{k})+\Lambda(\mathbf{k}) . \tag{B1}$$

Here, $L^E(\mathbf{k})$, $V(\mathbf{k})$, $M(\mathbf{k})$, and $\Lambda(\mathbf{k})$ are 2×2 matrix operators acting on two-dimensional vectors of the type $[f(\mathbf{v}_1),g(\mathbf{v}_2)]$ and transforming them into vectors of the same type $[f'(\mathbf{v}_1),g'(\mathbf{v}_2)]$, where $f(\mathbf{v}_1)$ and $g(\mathbf{v}_2)$ are arbitrary functions of $\mathbf{v}_1$ and $\mathbf{v}_2$, respectively.

The 2×2 free-streaming matrix operator $V(\mathbf{k})$ is given by

$$V(\mathbf{k})=\begin{bmatrix}-i\mathbf{k}\cdot\mathbf{v}_1 & 0\\ 0 & -i\mathbf{k}\cdot\mathbf{v}_2\end{bmatrix} . \tag{B2}$$

The 2×2 mean-field matrix operator $M(\mathbf{k})$ is given by

$$M(\mathbf{k})=\begin{bmatrix}M_{11}(\mathbf{k}) & M_{12}(\mathbf{k})\\ M_{21}(\mathbf{k}) & M_{22}(\mathbf{k})\end{bmatrix} . \tag{B3}$$

The four operators $M_{jl}(\mathbf{k})$ with j or $l=1,2$ transform functions of $\mathbf{v}_1$ into functions of $\mathbf{v}_j$. For an arbitrary function $f(\mathbf{v}_l)$ of $\mathbf{v}_l$, one has [10]

$$M_{jl}(\mathbf{k})f(\mathbf{v}_l)=\int d\mathbf{v}_3\phi^{(l)}(v_3)[i\mathbf{k}\cdot\mathbf{v}_j\delta s_{jl}(k)+i\mathbf{k}\cdot\mathbf{v}_3\delta s_{lj}(k)]f(\mathbf{v}_3) , \tag{B4}$$

with $\phi^{(l)}(v)$ the Maxwell velocity distribution of Eq. (9). The four functions $\delta s_{11}(k)$, $\delta s_{22}(k)$, $\delta s_{21}(k)$, and $\delta s_{12}(k)$ depend on the deviations of $S_{11}(k)$, $S_{12}(k)=S_{21}(k)$, and $S_{22}(k)$ from their ideal-gas values (1, 0, 1, respectively):

$$\delta s_{jj}(k)=1-[\bar{S}_{jj}(k)]^{-1/2}\cos\alpha(k) \tag{B5}$$

and

$$\delta s_{jl}(k)=[\bar{S}_{jj}(k)]^{-1/2}\sin\alpha(k) \quad (j\neq l) , \tag{B6}$$

with

$$\bar{S}_{jj}(k)=S_{jj}(k)\frac{S_{11}(k)S_{22}(k)-S_{12}(k)^2}{S_{11}(k)S_{22}(k)} \tag{B7}$$

and $\alpha(k)$ given by Eq. (11). Therefore, $\delta s_{jl}(k)=0$ and $M_{jl}(\mathbf{k})=0$ for ideal gases.

The collision operator $\Lambda(\mathbf{k})$ in Eq. (B1) is given by

$$\Lambda(\mathbf{k})=\begin{bmatrix}\Lambda_{11}(\mathbf{k}) & \Lambda_{12}(\mathbf{k})\\ \Lambda_{21}(\mathbf{k}) & \Lambda_{22}(\mathbf{k})\end{bmatrix} , \tag{B8}$$

where $\Lambda_{jl}(\mathbf{k})$ transforms functions $f(\mathbf{v}_l)$ of $\mathbf{v}_l$ into functions of $\mathbf{v}_j$, i.e.,

$$\Lambda_{jl}(\mathbf{k})f(\mathbf{v}_l)=\bar{\Lambda}_{jl}(\mathbf{k})f(\mathbf{v}_l)-\langle\bar{\Lambda}_{jl}(\mathbf{k})f(\mathbf{v}_l)\rangle_j . \tag{B9}$$

The four collision operators $\bar{\Lambda}_{jl}(\mathbf{k})$ are

$$\bar{\Lambda}_{11}(\mathbf{k})f(\mathbf{v}_1)=n_1\chi_{11}\int d\hat{\boldsymbol{\sigma}}\int d\mathbf{v}_1^{(3)}\phi^{(1)}(v_1^{(3)})C_{11}^{(13)}(\hat{\boldsymbol{\sigma}})\{f[\mathbf{v}_1^{(1)}]+e^{-i\mathbf{k}\cdot\boldsymbol{\sigma}_{11}}f[\mathbf{v}_1^{(3)}]\}$$
$$+n_2\chi_{12}\int d\hat{\boldsymbol{\sigma}}\int d\mathbf{v}_2^{(3)}\phi^{(2)}(\mathbf{v}_2^{(3)})C_{21}^{(31)}(\hat{\boldsymbol{\sigma}})f[\mathbf{v}_1^{(1)}] , \tag{B10}$$

$$\bar{\Lambda}_{22}(\mathbf{k})f(\mathbf{v}_2)=n_2\chi_{22}\int d\hat{\boldsymbol{\sigma}}\int d\mathbf{v}_2^{(3)}\phi^{(2)}(v_2^{(3)})C_{22}^{(23)}(\hat{\boldsymbol{\sigma}})\{f[\mathbf{v}_2^{(2)}]+e^{-i\mathbf{k}\cdot\boldsymbol{\sigma}_{22}}f[\mathbf{v}_2^{(3)}]\}$$
$$+n_1\chi_{12}\int d\hat{\boldsymbol{\sigma}}\int d\mathbf{v}_1^{(3)}\phi^{(1)}(\mathbf{v}_1^{(3)})C_{12}^{(32)}(\hat{\boldsymbol{\sigma}})f[\mathbf{v}_2^{(2)}] , \tag{B11}$$

and, for $j\neq l$.

$$\bar{\Lambda}_{jl}(\mathbf{k})f(\mathbf{v}_l)=(n_1n_2)^{1/2}\chi_{12}\int d\hat{\boldsymbol{\sigma}}\,e^{-i\mathbf{k}\cdot\boldsymbol{\sigma}_{12}}\int d\mathbf{v}_l^{(l)}\phi^{(l)}(v_l^{(l)})C_{jl}^{(jl)}(\hat{\boldsymbol{\sigma}})f[\mathbf{v}_l^{(l)}] , \tag{B12}$$

Here, $\hat{\boldsymbol{\sigma}}$ is a unit vector.

$$\boldsymbol{\sigma}_{jl}=\sigma_{jl}\hat{\boldsymbol{\sigma}} , \tag{B13}$$

$$\sigma_{jl}=(\sigma_j+\sigma_l)/2 , \tag{B14}$$

so that $\sigma_{11}=\sigma_1$, $\sigma_{22}=\sigma_2$, and $\sigma_{12}=(\sigma_1+\sigma_2)/2$. $\chi_{jl}=g_{jl}(\sigma_{jl})$, with $g_{jl}(r)$ the partial equilibrium pair-correlation functions of the mixture. In Eqs. (B10)–(B12), $\mathbf{v}_j^{(p)}$ is the velocity of particle number p of species $j=1,2$, and we set $\mathbf{v}_j^{(p)}=\mathbf{v}_j$ after the integrations have been performed.

The operator $C_{jl}^{(pq)}(\hat{\boldsymbol{\sigma}})$ describes the collision of particle p of species j with particle q of species l:

$$C_{jl}^{(pq)}(\hat{\boldsymbol{\sigma}})=\sigma_{jl}|\mathbf{v}_{jl}^{(pq)}\cdot\boldsymbol{\sigma}_{jl}|\Theta(\mathbf{v}_{jl}^{(pq)}\cdot\boldsymbol{\sigma}_{jl})[b_{jl}^{(pq)}(\hat{\boldsymbol{\sigma}})-1] , \tag{B15}$$

where $\Theta(x)$ is the Heaviside step function and

$$\mathbf{v}_{jl}^{(pq)}=\mathbf{v}_j^{(p)}-\mathbf{v}_l^{(q)} . \tag{B16}$$

The substitution operator $b_{jl}^{(pq)}(\hat{\boldsymbol{\sigma}})$ in Eq. (B15) acts on functions $f(\mathbf{v}_j^{(p)},\mathbf{v}_l^{(q)})$ of $\mathbf{v}_j^{(p)}$ and $\mathbf{v}_l^{(q)}$ as

$$b_{jl}^{(pq)}(\hat{\boldsymbol{\sigma}})f(\mathbf{v}_j^{(p)},\mathbf{v}_l^{(q)})=f(\mathbf{v}_j^{(p)*},\mathbf{v}_l^{(q)*}) , \tag{B17}$$

where

$$b_{jl}^{(pq)}(\hat{\boldsymbol{\sigma}})\boldsymbol{v}_j^{(p)}=\boldsymbol{v}_j^{(p)*}=\boldsymbol{v}_j^{(p)}-2\frac{\mu_{jl}}{m_j}[\boldsymbol{v}_{jl}^{(pq)}\cdot\hat{\boldsymbol{\sigma}}]\hat{\boldsymbol{\sigma}}\ , \tag{B18}$$

$$b_{jl}^{(pq)}(\hat{\boldsymbol{\sigma}})\boldsymbol{v}_l^{(q)}=\boldsymbol{v}_l^{(q)*}=\boldsymbol{v}_l^{(q)}-2\frac{\mu_{jl}}{m_l}[\boldsymbol{v}_{lj}^{(qp)}\cdot\hat{\boldsymbol{\sigma}}]\hat{\boldsymbol{\sigma}}\ , \tag{B19}$$

with the reduced masses μ_{jl} given by

$$\mu_{jl}=\frac{m_j m_l}{m_j+m_l}\ . \tag{B20}$$

The $\boldsymbol{v}_j^{(p)*}$ and $\boldsymbol{v}_l^{(q)*}$ in Eq. (B17) are the velocities after a binary collision of particles p and q when they have initial velocities $\boldsymbol{v}_j^{(p)}$ and $\boldsymbol{v}_l^{(q)}$, respectively.

[1] E. G. D. Cohen, P. Westerhuijs, and I. M. de Schepper, Phys. Rev. Lett. **59**, 2872 (1987).

[2] H. van Beijeren and M. H. Ernst, Physica **68**, 437 (1973); **70**, 225 (1973); J. Stat. Phys. **21**, 125 (1979).

[3] E. G. D. Cohen and I. M. de Schepper, Nuovo Cimento D **12**, 521 (1990).

[4] N. W. Ashcroft and D. C. Langreth, Phys. Rev. **156**, 685 (1967).

[5] V. A. Rabinovich, A. A. Vasserman, V. I. Nedostrup, and L. S. Veksler, *Thermophysical Properties of Neon, Argon, Krypton and Xenon* (Springer-Verlag, Berlin, 1988).

[6] V. V. Sychev, A. A. Vasserman, A. D. Kozlov, G. A. Spiridonov, and V. A. Tsymarny, *Thermodynamic Properties of Helium* (Springer-Verlag, Berlin, 1987).

[7] P. Verkerk and A. A. van Well, Nucl. Instrum. Methods Phys. Res. **228**, 438 (1985).

[8] J. P. Boon and S. Yip, *Molecular Hydrodynamics* (Dover, New York, 1991).

[9] J. R. Dorfman and H. van Beijeren, in *Statistical Mechanics B*, edited by B. J. Berne (Plenum, New York, 1977).

[10] I. M. de Schepper and W. Montfrooij, Phys. Rev. A **39**, 5807 (1989).

[11] A. Campa and E. G. D. Cohen, Phys. Rev. A **41**, 5451 (1990).

[12] I. M. de Schepper, E. G. D. Cohen, and B. Kamgar-Parsi, J. Stat. Phys. **54**, 273 (1989).

[13] C. Y. Ho, *Properties of Nonmetallic Fluid Elements* (Hemisphere, New York, 1989).

[14] P. Westerhuijs, W. Montfrooij, L. A. de Graaf, and I. M. de Schepper, Phys. Rev. A **45**, 3749 (1992).

[15] P. Westerhuijs, M. T. Besseling, L. A. de Graaf, and I. M. de Schepper, Physica B **182**, 302 (1992).

[16] J. S. Rowlinson, *Liquids and Liquid Mixtures* (Butterworth, London, 1969).